Solidification Cracking Susceptibility of Commercial Copper-Based Feedstocks

The Kou crack susceptibility index accurately ranked the measured solidification cracking behavior of commercial copper-based feedstocks using the Sigmajig test

BY J. KLEINDIENST, D. JAVERNICK, AND J. KLEMM-TOOLE

Abstract

Copper alloys offer an excellent balance of corrosion resistance and strength and are of interest for marine and other applications. Research on the mechanical properties and microstructure of welded and additively manufactured copper-based alloys has been conducted; however, further work is needed to understand their susceptibility to solidification cracking. The weldability of six commercially available wire feedstocks deposited with gas metal arc directed energy deposition was evaluated using the Sigmajig weldability test. Full-penetration autogenous gas tungsten arc remelts were performed at various applied stresses, and solidification cracking was measured. At an applied stress of 10 MPa, the alloys were ranked from most to least weldable as follows: ERCuAl, ERCuNiAl, ERCuMnNiAl, ERCuNi, ERCuSi, and ERCu. The Kou crack susceptibility index (CSI) was applied to these compositions, and the CSI ranking matched the Sigmajig ranking of cracking susceptibility. Fractography showed dendrites on the fracture surface in all samples, confirming solidification cracking, except in ERCuAl samples, which exhibited extensive microvoid coalescence, indicating significant plastic deformation before sample failure. This work provides a deeper understanding of solidification cracking behavior, which will inform alloy selection and cracking mitigation in the growing field of additive manufacturing using copper-based feedstocks.

https://doi.org/10.29391/2026.105.025

Keywords

- Copper
- Weldability
- Gas Metal Arc Directed Energy Deposition
- Gas Tungsten Arc Welding
- Wire Arc Additive Manufacturing
- Solidification Modeling

Introduction

Copper alloys are of interest to the marine industry for their combination of mechanical properties and corrosion resistance. Extensive research has been conducted on additively manufactured (AM) bronze alloys for naval applications; however, solidification cracking in copper alloys remains a concern that has not been adequately addressed in the welding or AM literature. The copper alloy that has received the most welding research is nickel-aluminum bronze (NAB), an alloy that shows promise for the production of propellers through additive manufacturing. Significant literature exists on the complex solid-state phase transformations in NAB and their effects on mechanical properties under a wide range of processing conditions (Refs. 1–9). Li et al. observed the presence of hot cracks in blown powder laser AM at high laser powers in NAB (Ref. 10). Bellware studied the effects of residual amounts of phosphorus and lead on the weldability of NAB; however, no additional weldability data can be found comparing the weldability of NAB to other copper alloys (Ref. 11). A similar alloy that has received interest in naval applications is manganese nickel bronze, an alloy that offers mechanical properties similar to NAB, however no weld cracking research exists on it (Refs. 12, 13).

Additional copper alloys are of interest also due to their potential naval applications. 70/30 Cu/Ni is an alloy that has been studied for marine part production and repair, and work

Table 1 — Chemical Compositions of Alloys Studied

	Cu	Al	Ni	Si	Mn	Zn	Sn	Fe	C	N
ERCu	Bal	0.02	0.06	0.33	0.27	0.01	0.82	0.01	<0.01	0.057
ERCuSi	Bal	0.01	0.19	2.91	0.79	0.01	0.01	0.05	<0.01	<0.01
ERCuNi	Bal	0.03	28.90	0.02	0.83	0.24	<0.01	0.80	0.026	<0.01
ERCuMn-NiAl	Bal	7.21	2.06	<0.01	11.41	<0.01	<0.01	2.68	0.018	<0.01
ERCuNiAl	Bal	8.81	5.52	0.04	0.97	0.01	<0.01	4.80	0.011	0.063
ERCuAl	Bal	8.42	<0.01	<0.01	0.01	0.01	<0.01	0.54	<0.01	0.077

has been done to examine the effects of process selection and parameters on the mechanical properties of the depositions (Refs. 14–16). Garriott tested aluminum-bronze alloys using a circular patch test and found that ERCuAl exhibited excellent weldability compared with other aluminum-bronze alloys (Ref. 17). Aluminum-bronze alloys have been proposed as a solution for iron-to-copper dissimilar joining (Refs. 18, 19). In addition to the alloys mentioned above, silicon bronze and high-thermal-conductivity copper alloys are also commercially available, but only a limited amount of weldability data is available in the literature. The AWS Welding Handbook Vol. 5, and Welding Research Bulletin 287 offer guidelines for filler metal selection, joint preparation, and welding parameters; however, there is a lack of published research on the susceptibility of these alloys to solidification cracking (Refs. 20, 21). Overall, to implement copper-based feedstocks for AM or other welding applications for structural parts, more work is needed to experimentally evaluate weldability and the predictive capability of solidification cracking models for copper alloys.

The Sigmajig weldability test applies an initial uniaxial stress to a sheet sample perpendicular to an autogenous, full-penetration weld. Modeling work done by Feng et al. shows that this stress state behind the moving melt pool evolves with time and position during the test (Ref. 22). Tests are conducted and cracking is measured at a range of imposed stresses, allowing the creation of a "cracking curve," which tracks the cracking behavior of an alloy over a range of applied stresses that mimics constraint or tensile stresses that a weldment or AM build might experience. Alloys can be ranked by weldability, and design choices can be made based on these rankings. This test is not meant to simulate the specific stress states of a weld, but rather to induce solidification cracking and to compare cracking across different alloys in a repeatable way. Typically, the amount of cracking is defined as the longest optically observed crack length divided by the length of the weld (Refs. 23–25). This test has been applied to steel, stainless steel, and aluminum alloy systems (Refs. 23, 26–28, 25).

In addition to experimentally evaluating weldability, models that can rank the relative susceptibility to cracking amongst candidate copper alloys are desirable. Kou's cracking susceptibility index incorporates the Scheil solidification curve of an alloy and creates a simple metric that ranks solidification cracking susceptibility (Refs. 29, 30). This model has proven useful across a variety of alloy systems, including aluminum and iron alloys; however, there is a lack of literature on its application to copper alloy systems (Refs. 23, 24, 31, 32).

The purpose of this work is to rank six different common copper alloys in terms of weldability, more specifically, solidification cracking susceptibility. Samples of each copper feedstock were printed using gas metal arc directed energy deposition (GMA-DED) and tested with the Sigmajig using full-penetration autogenous gas tungsten arc (GTA) remelt tracks. The remelt microstructures were characterized via light optical microscopy. Fractography was performed to confirm the cracking mechanism. The Kou crack-susceptibility index (CSI) was determined for each alloy and compared with the cracking results from the Sigmajig test. The results of this study are expected to enable alloy selection for welding and AM applications and facilitate future weldability research of copper alloys.

Methodology Introduction

Copper alloys are of interest to the marine industry for their combination of mechanical properties and corrosion resistance. Extensive research has been conducted on AM bronze alloys for naval applications; however, solidification cracking in copper alloys remains a concern that has not been adequately addressed in the welding or AM literature. The copper alloy that has received the most welding research is NAB, an alloy that shows promise for the production of propellers through additive manufacturing. Significant literature exists on the complex solid-state phase transformations in NAB and their effects on mechanical properties under a wide range of processing conditions (Refs. 1–9). Li et al. observed the presence of hot cracks in blown powder laser AM at high laser powers in NAB (Ref. 10). Bellware studied the effects of residual amounts of phosphorus and lead on the weldability of NAB; however, no additional weldability data can be found comparing the weldability of NAB to other copper alloys (Ref.

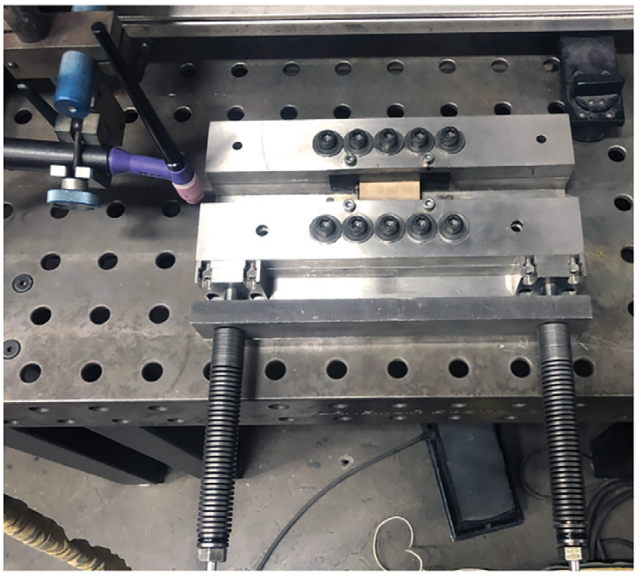


Fig. 1 — Photo of Sigmajig experimental setup.

11). A similar alloy that has received interest in naval applications is manganese nickel bronze, an alloy that offers

Test Sample Fabrication

Samples were made by GMA-DED printing single-bead-wide walls. Walls were fabricated using commercially available copper-based welding wires with compositions shown in Table 1, as determined by optical emission spectroscopy (OES) and combustion compositional analysis of as-printed GMA-DED builds. The compositional test of the ERCuMnNiAl GMA-DED was contaminated, so the wire composition is reported in Table 1. Elemental loss during welding is a concern; however, no significant elemental loss was found between the wire and GMA-DED compositions. The presence of Sn in ERCu is typical and will be discussed later in the manuscript. A six-axis collaborative robot-controlled Fronius TPS400i GMAW power source deposited the walls onto bronze base plates. All wires had a diameter of 0.045 in. and 100% Ar shielding gas was used at a flow rate of 11.3 L/min (30 ft^3/hr), and a travel speed of 12 mm/s (28.3 in./min) was used for all builds. A pulse multi-control (PMC) transfer mode was used to deposit the ERCu wire due to its higher thermal conductivity, with a wire feed speed (WFS) of 99.5 mm/s (235 in./min) and a voltage of 20.2 V. The rest of the 5 copper alloys were deposited with a cold metal transfer (CMT) mode and a WFS of 74.1 mm/s (175 in./min) and a voltage of 10.8 V. AM walls were cut from the bronze base plate and machined into 2 mm thick plates and sectioned into 2 in. × 2 in. sections for weld testing.

Weldability Experimentation

Weldability tests were conducted using the Sigmajig test equipment (Fig. 1) and a Miller Dynasty® 350 power source on a motorized track. Full-penetration, autogenous GTA remelts were performed on the machined copper alloy samples while the samples were preloaded with a restraint load transverse to the welding direction. The samples were always oriented so that the GTA remelt ran perpendicular to the original GMA-DED build direction. This was done to minimize the influence of potential cracks in the samples on the Sigmajig test results. Each remelt was made with a 2.38 mm (3/32 in.) tungsten electrode, 1 mm standoff distance from the sample surface, 100% Ar shielding gas at a flow rate of 11.3 L/min (30 ft^3/hr), and a travel speed of 12 mm/s (28.3 in./min). The tungsten standoff distance was measured using a 1-mm-thick plate to minimize voltage differences between tests. Welding amperage varied for each alloy to achieve a full penetration remelt and were as follows: ERCu: 230A; ERCuSi: 160A; ERCuNi: 220A; ERCuMnNiAl: 140A; ERCuNiAl: 175A; and ERCuAl: 160A. These parameters created a teardrop-shaped melt pool, the standard melt pool geometry for the Sigmajig weldability test (Ref. 33). Sample thickness and length were measured prior to testing and used to calculate the cross-sectional area of each sample.

Remelts were conducted at a range of transverse loads to build out cracking behavior curves from no load to full separation of the sample. After the test was conducted, each sample was allowed to cool, and the crack length was measured using optical microscopy on the top surface of the remelt. The length of the longest crack was measured and divided by the length of the remelt to give a percent cracking metric for each test, ranging from zero (no crack) to one hundred (full separation of the remelt during testing). The stress for each test was calculated by dividing the imposed load by the cross-sectional area of the test plate.

Solidification Cracking Modeling

A solidification-cracking criterion proposed by Kou was used to rank the alloys by weldability. The Kou CSI uses temperature over the square root of volume fraction solid data found through a Scheil simulation (Refs. 29, 30). During the solidification of the melt pool, the contraction of the adjacent solid imposes a tensile strain on the evolving solid phase. The resulting dendritic separation is backfilled by available liquid as solidification progresses, until the fraction of liquid is insufficient, at which point dendritic separation can cause cracks. The CSI combines these processes into a single metric that gauges an alloy's susceptibility to solidification cracking. The CSI is defined as the maximum slope of the temperature vs. square root of the fraction solid ($f_s^{½}$) in the range of $0.85 < f_s^{½} < 0.99$. ThermoCalc® Scheil simulations were made of the compositions listed in Table 1 using the HEA7.0 database, and the alloys were ranked in terms of their predicted weldability. The Kou CSI has not been traditionally applied to copper alloys, so its implementation in this study offers new data for its applicability to new alloy systems.

In addition to simulating each individual alloy, Scheil simulations of binary Cu alloys with major alloying elements were performed over a range of compositions. Compositions of Cu alloyed with Sn, Si, Mn, Al, Fe, and Ni between 0 and 10 wt-% were input into ThermoCalc® Scheil simulations using the HEA7.0 database, and the Kou cracking index was calculated for each composition. The cracking susceptibility

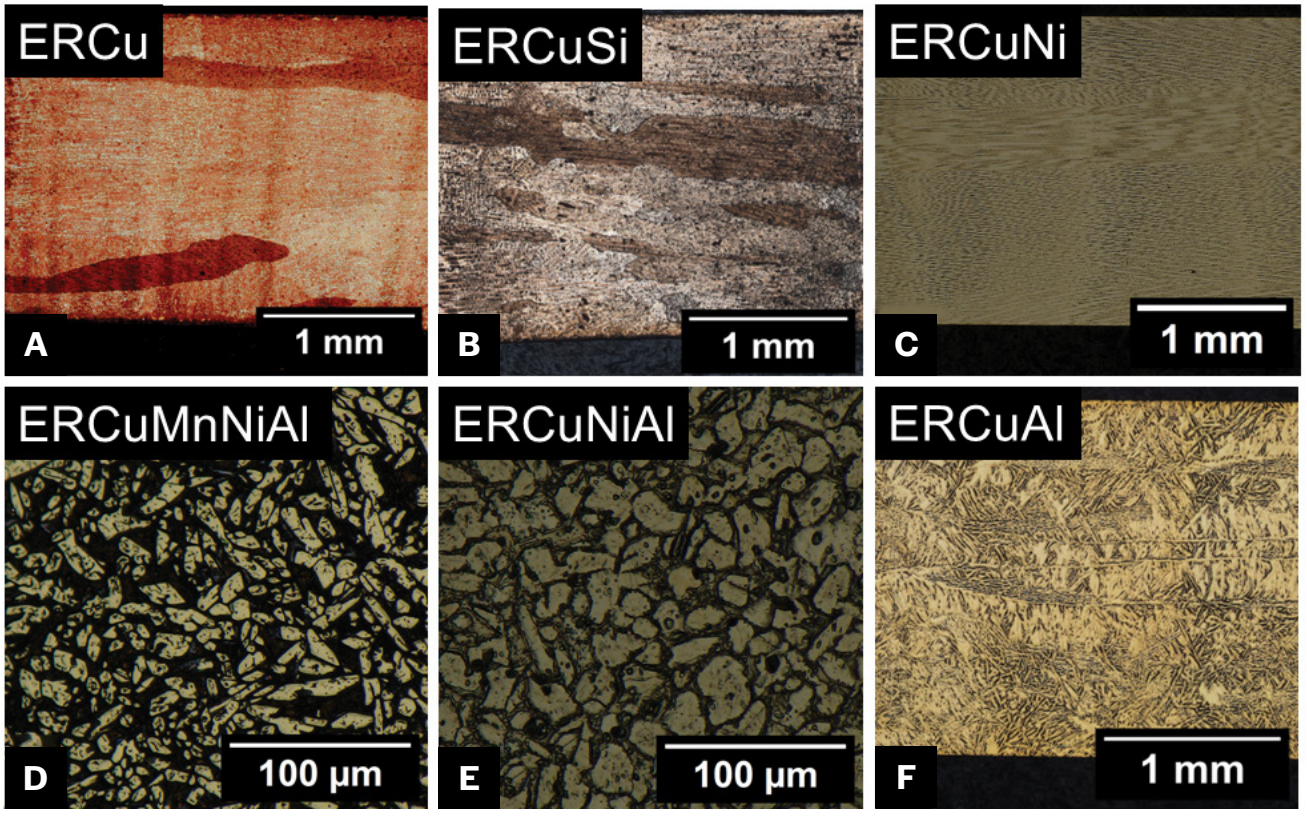


Fig. 2 — Etched light optical micrographs of transverse cross-sectioned GMA-DED builds of: A — ERCu; B — ERCuSi; C — ERCuNi; D — ERCuMnNiAl; E — ERCuNiAl; F — ERCuAl (build direction is left to right).

results across compositions will provide broader context for the weldability of each alloy studied.

Microstructure Characterization

After Sigmajig testing at zero stress, samples of each alloy were sectioned and mounted transverse to the remelt direction. Samples were polished to a 1 µm diamond finish, and then chemically etched to reveal their microstructure. The ERCu, ERCuSi, and ERCuAl samples were immersed in an etchant solution of 50 mL HNO_3, 50 mL H_2O, and 0.5 g $AgNO_3$ for roughly 10 s. The ERCuMnNiAl and ERCuNiAl samples were immersed in a solution of 3 g $FeCl_3$, 5 mL HCl, and 100 mL H_2O for roughly 10 s. An etchant solution of 10 mL HCl, 1 g $FeCl_3$, and 100 mL H_2O was used to etch ERCuNi by immersion for approximately 10 s. The etched samples were optically imaged with an Olympus DSX 500 digital light optical microscope to observe the microstructure of the GTA remelt and GMA-DED build. Fracture surfaces of fully cracked remelts of each alloy were imaged by an FEI Helios Nanolab 600i scanning electron microscope (SEM) at 15 keV beam energy and 5.5 nA beam current to observe the cracked fracture surface features.

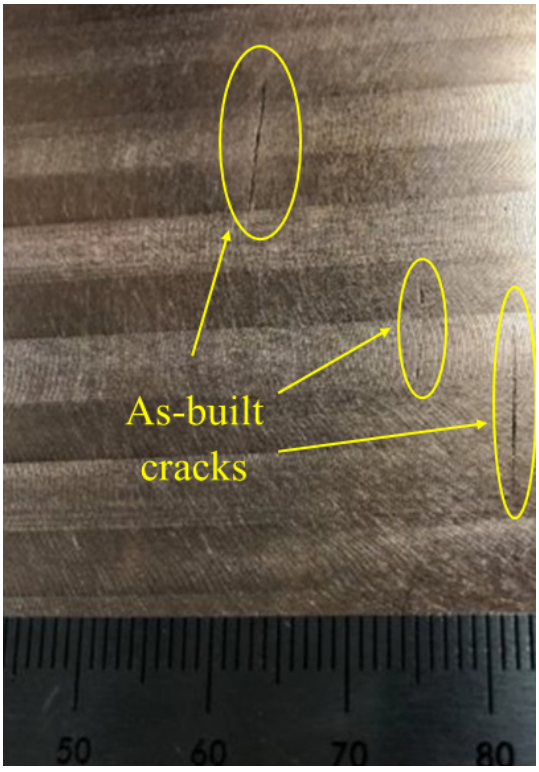


Fig. 3 — Optical image of the machined surface of the as-built GMA-DED ERCu plate (build direction is aligned vertically).

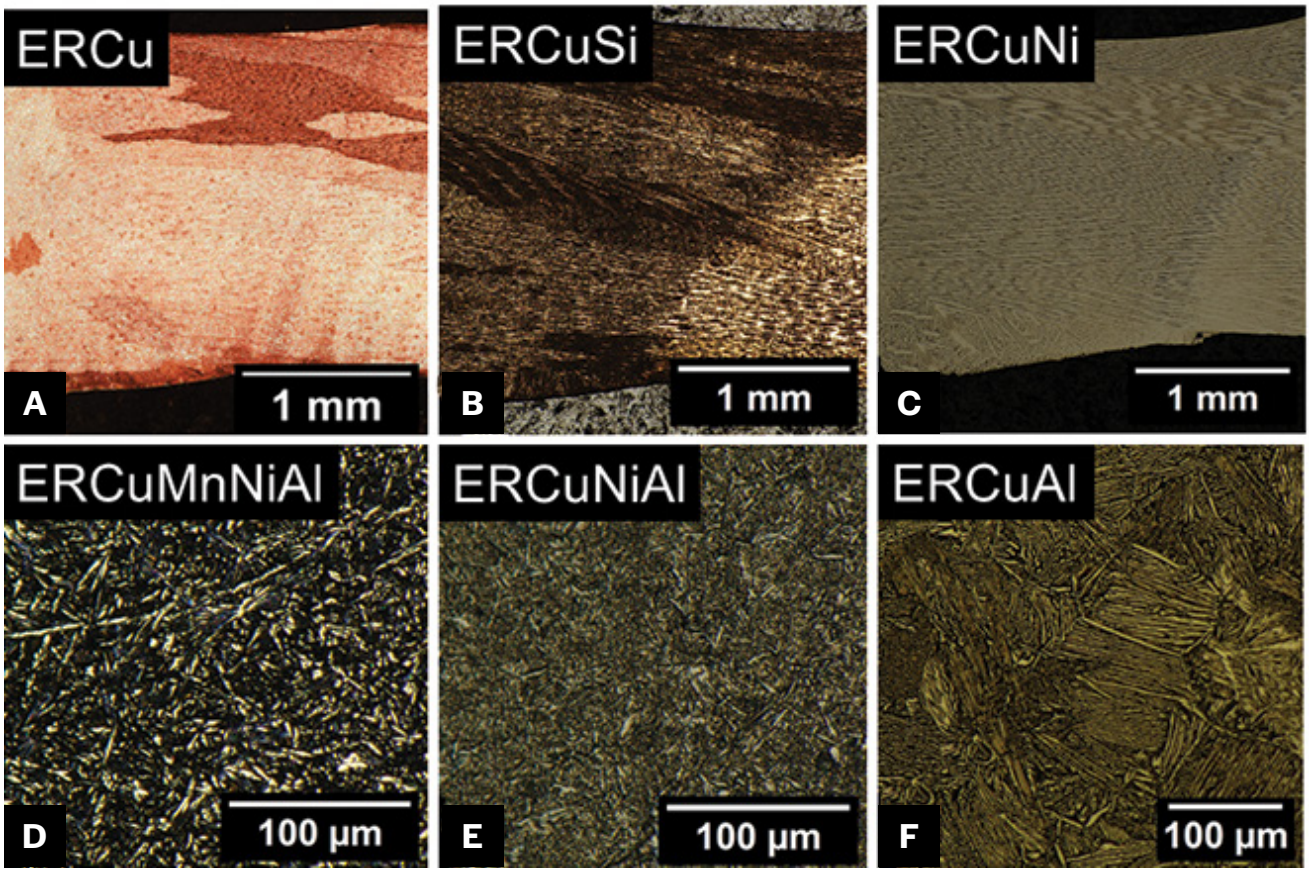


Fig. 4 — Etched light optical micrographs of transverse cross-sectioned GTA remelts of: A — ERCu; B — ERCuSi; C — ERCuNi; D — ERCuMnNiAl; E — ERCuNiAl; F — ERCuAl.

Results

Sample Microstructure

Figure 2 shows the etched microstructures of the GMA-DED prints of each of the copper alloys, with the build direction on the horizontal axis. ERCu, ERCuSi, and ERCuNi (Figs. 2A–C) showed coarse, columnar grains with dendritic solidification patterns extending along the build direction. The solidification grain size of ERCu was coarser than that of ERCuSi and ERCuNi, likely due to the increased alloy content in ERCuSi and ERCuNi and corresponding increased undercooling during solidification. The aluminum-containing alloys (ERCuMnNiAl, ERCuNiAl, and ERCuAl) all exhibited evidence of solid-state transformations, obscuring the solidification microstructures. The etched micrograph of ERCuAl in Fig. 2F displayed a coarse, acicular microstructure with grain boundaries oriented along the build direction. Based on published literature of welded microstructures of the NAB alloy (Refs. 1, 3), it appeared that ERCuNiAl (Fig. 2E) contains a matrix of light etched alpha (α) phase surrounded by a dark etched intergranular network of a combination of α phase and various fine kappa (κ) precipitates. The ERCuMnNiAl micrograph in Fig. 2D showed a similar microstructure to ERCuNiAl with a light phase identified as α and intergranular dark phase identified as β by Guo et al. (Ref. 12). No cracks or porosity were observed in any of the etched GMA-DED microstructures; however, significant cracks (2-5 mm) were observed on the as-machined surface of the GMA-DED ERCu plates along the building direction, pictured in Fig. 3. Given the large size (~10 mm) and orientation of cracks along the build direction of the plate, it is likely that these were solidification cracks that initiated along the centerline of the GMA-DED melt pool and grew through several build layers.

Etched microstructures of the GTA remelted fusion zone of each alloy are displayed in Fig. 4. Each of these samples were tested in the Sigmajig at zero applied load. No cracking or porosity was observed in any of the cross sections taken from the remelts. ERCu, ERCuSi, and ERCuNi, as seen in Figs. 4A–C, exhibited a similar microstructure to that observed in the GMA-DED builds in Fig. 2, with large, columnar grains containing dendritic solidification patterns extending throughout the melt pool. Evidence for epitaxial growth was evident in each of these remelt microstructures, with grains extending from the GMA-DED base material into the GTA remelt and then growing competitively to the melt pool centerline.

As with the GMA-DED microstructures, GTA remelts of the aluminum-containing alloys (Figs. 4D–F) displayed a solid-state-transformed microstructure that overwrote the solidification structure. Significant refinement of the microstructure was seen in both the ERCuMnNiAl and ERCuNiAl GTA remelts compared to the GMA-DED microstructures, and there was a more prevalent needle morphology of the presumed α phase in the GTA remelt microstructures. The

ERCuAl micrograph in Fig. 4F showed a fine basket-weave morphology, a shift from the microstructure observed in the GMA-DED build. These changes in the microstructure length scale and morphology of the aluminum-containing copper alloys can be attributed to the significantly higher preheat and melt pool size in the GMA-DED builds compared to the GTA remelts, leading to faster cooling rates in the GTA remelts and changes in solid-state phase transformations. It should be noted that these solid-state phase transformations do not affect the susceptibility of the alloys to solidification cracking, as they occur after solidification is complete; however, they can significantly impact the mechanical properties of these alloys.

Weldability Testing

Sigmajig weldability results for each alloy across a range of imposed stresses were plotted in Fig. 5. Most of the alloys exhibited similar behavior, with a minor amount of cracking (< 20%) at low stresses that increased slowly with stress and then transitioned sharply to full cracking above a critical stress value. The only alloy that did not follow this trend was ERCuAl, which exhibited no cracking up to high stresses (> 130 MPa) and then sharply transitioned to full cracking above 140 MPa, placing its weldability well above that of every other alloy. The other two aluminum-containing alloys performed well in weldability testing, with ERCuNiAl showing the least cracking among the four copper alloys. Based on the cracking curves in Fig. 5, the alloys may be ranked from least to most weldable as follows: ERCu, ERCuSi, ERCuNi, ERCuMnNiAl, ERCuNiAl, and ERCuAl.

Due to experimental variation in the Sigmajig data shown in Fig. 5, additional samples of each alloy were tested at the same stress to directly compare their cracking results. The samples were tested at 10 MPa to induce the widest range of cracking behaviors in each alloy without causing full separation of the samples. The results of these tests were plotted in Fig. 6. The Sigmajig cracking results at 10 MPa matched the trends across the whole range of stresses tested, including the same order of the knees of the Sigmajig curves in Fig. 5, ranking the alloys in the same order of weldability.

Fractography

To confirm the cracking mechanism for each alloy that was Sigmajig tested, SEM fractography was conducted on the cracked fracture surface of a fully separated specimen of each alloy. The SEM images for each alloy were compiled in Fig. 7. Solidification cracking can be identified by the presence of dendrites on the fracture surface, as this feature confirms that separation of liquid films during solidification was the cause of cracking. As seen in Fig. 7, the fracture surface of every alloy other than ERCuAl contained dendrites, confirming that fracture was dominated by solidification cracking.

For ERCuAl, however, the fracture surface was dominated by microvoid coalescence (MVC), as shown in Fig. 4G, indicating ductile yielding of the material — an indication of exceptionally high solidification cracking resistance. This point was further confirmed by the reduction in cross-

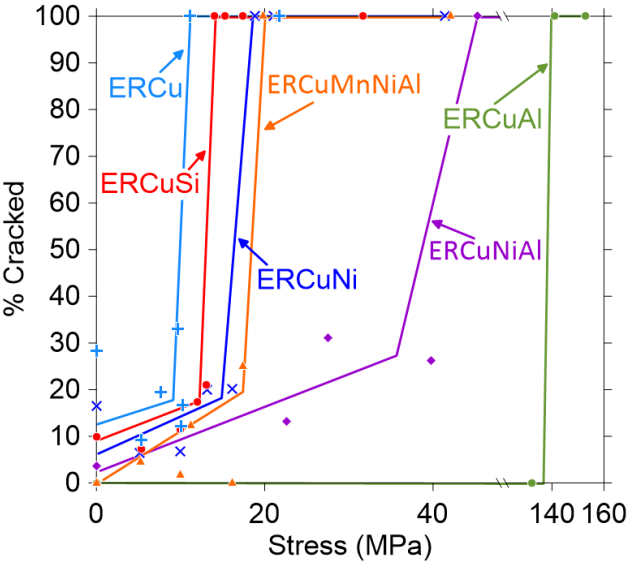


Fig. 5 — Results of Sigmajig testing plotted as percent cracking versus applied stress. Note the break in the horizontal axis where ERCuAl only shows any appreciable cracking close to 140 MPa.

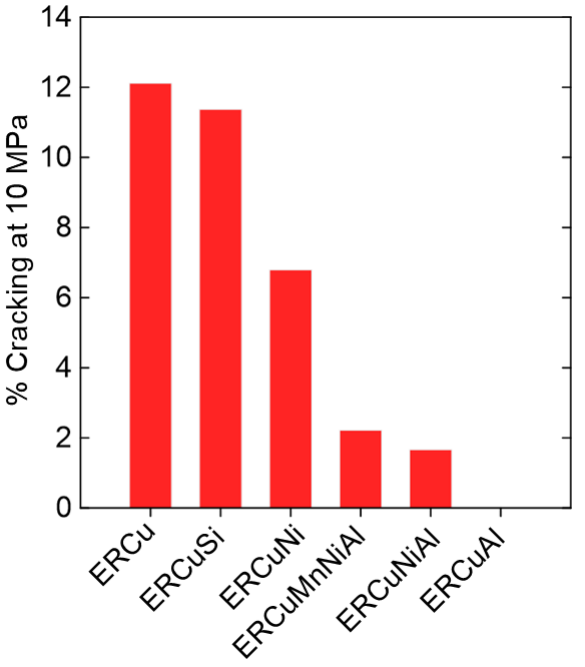


Fig. 6 — Comparison of the amount of cracking at an applied stress of 10 MPa.

sectional area of the ERCuAl samples in the remelt region at higher loads, and a noticeable load drop was recorded on the Sigmajig strain gage bolts after testing ERCuAl. There was a small region of dendrites on the ERCuAl fracture surface shown in Fig. 7F, located just before the remelt end crater, showing that some solidification cracking occurred, likely induced by the stress concentration of the yielded remelt region, creating a notch and stress concentration near the end of the remelt. A similar fracture behavior was observed

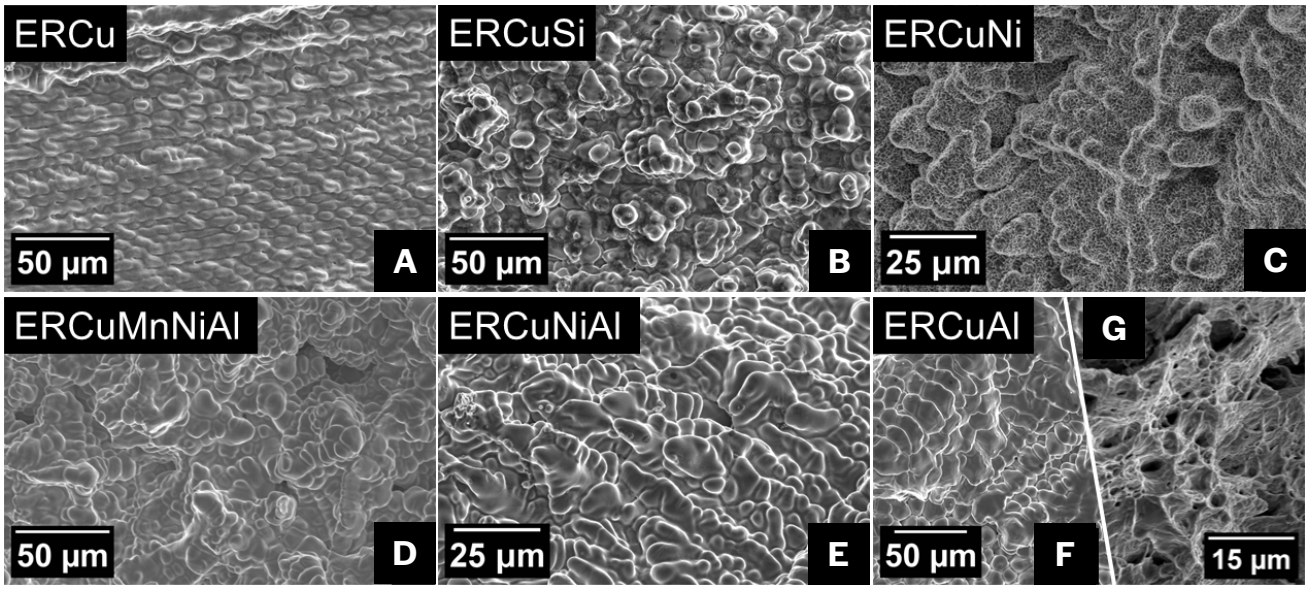


Fig. 7 — SEM images of failed Sigmajig sample fracture surfaces showing dendrites in: A — ERCu; B — ERCuSi; C — ERCuNi; D — ERCuMnNiAl; E — ERCuNiAl; F — ERCuAl; G — additional microvoid coalescence in ERCuAl.

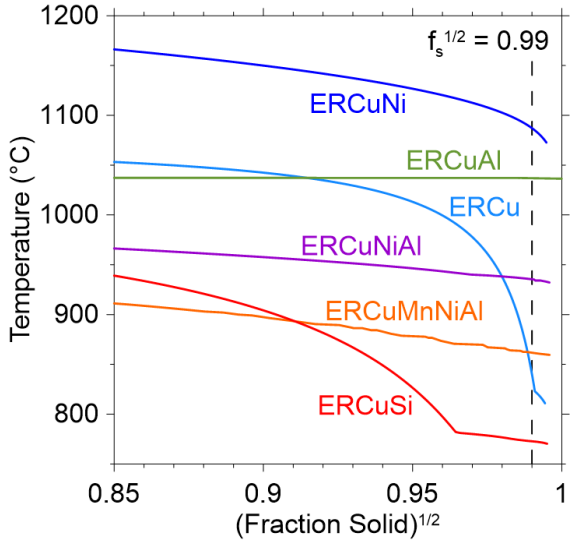


Fig. 8 — Overlaid Kou Scheil terminal solidification curves for each alloy.

by Geerlings et al. on Sigmajig samples of highly crack-resistant carbon steel (Ref. 19). From these observations, the excellent weldability of ERCuAl, as seen in Fig. 6, was limited by its high-temperature toughness. Overall, the SEM fractographs showed that each alloy experienced solidification cracking; however, the failure of ERCuAl was dominated by yielding, while the other alloys were dominated by solidification cracking.

Solidification Cracking Susceptibility Modeling

The temperature vs. square-root fraction solid during solidification, as determined by Scheil simulation, was plotted in Fig. 8. The solidification temperature ranges for each alloy varied by a few hundred degrees Celsius; however, the slope of the curve at terminal solidification is more relevant to its weldability than the solidification temperature range. The critical range for solidification cracking is between 0.85 and 0.99 $f_s^{1/2}$, since below 0.85 $f_s^{1/2}$ there is ample liquid available to backfill cracks, and above 0.99 $f_s^{1/2}$ the dendrites are sufficiently bonded to accommodate shrinkage strains (Refs. 29, 30).

ERCu had by far the steepest Scheil curve slope and corresponding highest shrinkage strains during solidification, suggesting that it was the least weldable of the alloys in question. ERCu is followed by ERCuSi and ERCuNi, both of which have steep Scheil-curve slopes and are associated with poor predicted weldability. It is interesting to note that ERCuNi is essentially a binary alloy of Cu and Ni and is predicted to solidify as a single face-centered cubic (FCC) phase throughout the relevant solidification window; however, it was still predicted to have poor weldability due to its partitioning behavior during terminal solidification.

Finally, the aluminum-containing bronze alloys exhibited relatively linear Scheil curves during terminal solidification and were predicted to be more weldable than the other alloys. ERCuAl especially had essentially no temperature drop during terminal solidification with a flat Scheil curve, meaning there were little to no thermal contraction strains on the network of dendrites at the end of solidification. This result indicated that it would be very weldable, which closely agreed with the experimental data, in which the weldability of ERCuAl was found to be driven by its high-temperature toughness rather than by susceptibility to solidification cracking.

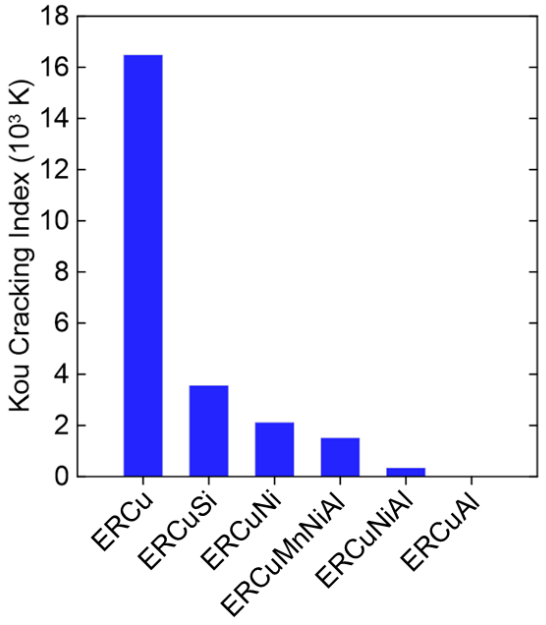


Fig. 9 — Kou cracking susceptibility indexes for each alloy.

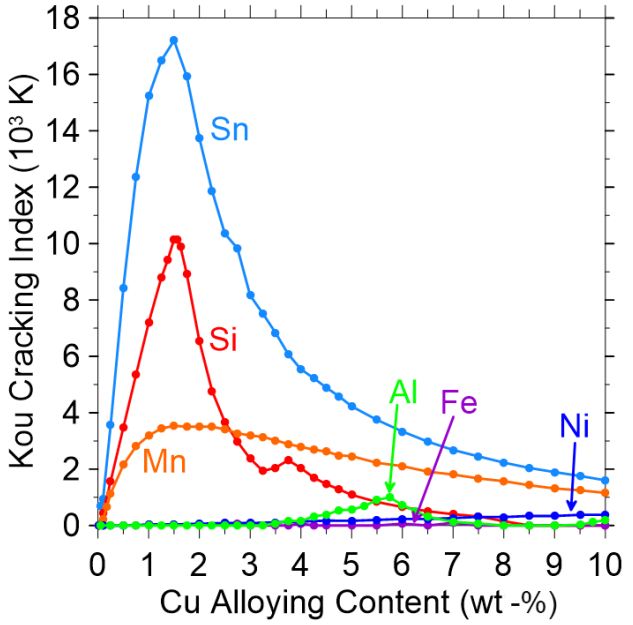


Fig. 10 — Kou cracking susceptibility curves of binary Cu alloys.

Table 2 — Minimum Mechanical Properties of All Metal Samples (Ref. 34)

ERCu	ERCuSi	ERCuNi	ERCuMnNiAl	ERCuNiAl	ERCuAl
170	350	350	520	500	410
20%	20%	20%	15%	10%	20%

The Scheil curves reported here gave a graphical expression of the solidification of the alloys in question and helped visualize the modeled weldability of each alloy. The Kou CSI values calculated from the Scheil curves shown in Fig. 8 were plotted in Fig. 9. The higher the CSI, the more prone to solidification cracking an alloy was predicted to be. ERCu had by far the worst predicted weldability, matching the steep Scheil curve in Fig. 8, followed by ERCuSi, ERCuNi, ERCuMnNiAl, ERCuNiAl, and finally ERCuAl, which had a cracking index close to zero. The ranking of these alloys agreed with the experimental weldability results in Fig. 6, a significant result that showed the Kou cracking index model can successfully model the weldability behavior of copper alloys. This agreement represented new data, as the Kou cracking criterion has primarily been applied to aluminum, ferrous, and nickel alloy systems, with little to no data on copper-based systems.

There was significant variation between the predicted and experimental weldability of ERCu. This was likely due to the Kou index prediction for ERCu falling on the boundary of the solidification window, where cracking was possible (the steepest part of the ERCu Scheil curve is right on the $f_s^{1/2} = 0.99$ dotted line). This $f_s^{1/2} = 0.99$ value is correlated to interdendritic bonding occurring in the fusion zone, and it is possible for bonding to occur before $f_s^{1/2} = 0.99$ (Ref. 24). If this were the case, the cracking index for ERCu would be much lower and correlate more closely to the observed cracking behavior. This result helped advance the fields of solidification modeling and research on copper weldability.

Kou's cracking index values for binary Cu alloys over a range of compositions were compiled and plotted in Fig. 10. It is evident that Sn had the most dramatic effect on cracking susceptibility among the alloying elements modeled, followed by Si and then Mn. Al showed very little effect on cracking susceptibility except for a small peak at 5.5 wt-%, and Fe exhibited no effect on the weldability of Cu. In the compositional window of 0-10 wt-%, Ni appeared to have only a minor impact on Cu cracking susceptibility; however, it steadily increased the Kou index with increasing alloying, and this trend continued past 10 wt-% Ni, explaining the poor weldability of ERCuNi, which contains about 30 wt-% Ni. This modeled cracking data for binary alloys is useful for understanding the effect of individual alloying elements on Cu weldability; however, additional modeling and experimental testing should be conducted for specific nonbinary compositions rather than combining the individual binary curves.

Discussion

Effects of Terminal Solidification

The results of the Kou cracking index model help explain the cracking behavior of the copper alloys considered. The cracking behavior of each alloy is tied to its terminal solidification profile. When an alloy has a solidification sequence that ends with a near-isothermal reaction, as in ERCuAl, it is highly resistant to solidification cracking. Conversely, it was initially hypothesized that ERCuNi would be very weldable due to the simplicity of its alloy system; however, it was found that the partitioning behavior of Ni in the alloy leads to considerable strains during terminal solidification and subsequent solidification cracking.

Individual Effects of Alloying Elements

Revisiting the cracking susceptibility curves in Fig. 10 helps explain the observed weldability of each feedstock. The potent effect of Sn on Cu cracking susceptibility drives the poor weldability of ERCu, which contains around 0.8 wt-% Sn. Minor additions of around 0.3 wt-% of Si and Mn each also contribute to its poor weldability. Behind Sn in terms of cracking susceptibility effect is Si, which peaks at around 2 wt-% Si. This explains the poor weldability of ERCuSi, which contains around 3 wt-% Si; if that amount were any lower, the feedstock would have even worse weldability. Even though Mn has a significant impact on Cu cracking tendency, ERCuMnNiAl has good weldability because it contains a large amount of Al and Fe, which help offset the presence of Mn in the alloy. The excellent weldability of ERCuAl is also explained by Fig. 9, which shows essentially no cracking susceptibility for a CuAl alloy at 8.5 wt-% Al.

Implications for Copper Feedstock Selection

In reviewing the weldability data presented in this study, it is worth discussing other relevant metrics in the selection process for a copper alloy. If solidification cracking susceptibility was the only relevant parameter in copper alloy welding and AM applications, ERCuAl would be the clear choice; however, in practice, it is not widely used in structural applications. The largest application space for these copper alloys is the production and repair of parts for marine applications, so the discussion will focus on this sector. In addition to weldability, the strength and ductility of copper alloys are important parameters that will be considered.

According to the AWS A5.6 (Ref. 34) specification on copper alloy welding wires, the minimum required tensile strength and elongation for all weld metal samples are shown in Table 2. Reviewing these properties, ERCu has the lowest strength as well as the worst weldability, and its use should be applied only to applications where restraint is low, preheat is used, and high thermal conductivity is required. ERCuSi and ERCuNi have identical mechanical property requirements and significantly lower strength than the aluminum bronzes. Given their limited weldability, their use in structural applications should be limited unless another parameter, such as corrosion resistance, is dominant in design considerations.

Despite its excellent weldability, ERCuAl has lower strength than ERCuNiAl and ERCuMnNiAl, which explains its limited research and use in structural applications. Accordingly, if solidification cracking is a persistent issue in applications, ERCuAl should be strongly considered, given its excellent weldability despite its lower but acceptable mechanical properties. Finally, ERCuMnNiAl and ERCuNiAl have very similar mechanical properties, although ERCuMnNiAl is slightly stronger and more ductile than ERCuNiAl. Given this moderate increase in mechanical properties, ERCuMnNiAl is a strong candidate for additional research in GMA-DED and other AM applications despite its slightly lower weldability compared to ERCuNiAl. The results of the weldability tests performed here provide key data to inform alloy selection for welding and AM applications and to prevent cracking.

Conclusions

Weldability of commercially available copper-based wire feedstocks was evaluated using the Sigmajig test. The Kou cracking susceptibility index was applied to the alloys and ranked their predicted weldability. SEM imaging of the crack surfaces and optical imaging of etched cross sections of the GMA-DED plates and GTA remelts were conducted. The following conclusions were made based on the results:

- Commercially available copper wires were ranked from least to most weldable in the following order by Sigmajig testing: ERCu, ERCuSi, ERCuNi, ERCuMnNiAl, ERCuNiAl, ERCuAl.
- Each crack fracture surface was found through SEM to be dominated by dendrites except for ERCuAl. This result shows that solidification cracking was the failure mechanism for each alloy except for ERCuAl, where the fracture surface was dominated by microvoid coalescence, showing a yielding failure. A small region of dendrites on the ERCuAl fracture surface was found near the end of the weld, indicating that the yielding crack notch induced solidification cracking at concentrated loads.
- The Kou CSI modeling results agreed with the experimentally determined weldability ranking of the alloys, confirming that the model can be applied to copper alloys.
- The results of this study are expected to enable copper feedstock selection as well as decrease the risk of solidification cracking for copper-based welding and AM applications.

Acknowledgements

The authors acknowledge support from the Manufacturing and Materials Joining Innovation Center (Ma^2JIC), a National Science Foundation Industry/University Cooperative Research Center (I/UCRC), and Award No. 2052819/LA-UR-25-32236 at the Colorado School of Mines.

References

1. Dharmendra, C., Hadadzadeh, A., and Amirkhiz, B. 2019. Microstructural evolution and mechanical behavior of nickel aluminum

bronze Cu-9Al-4Fe-4Ni-1Mn fabricated through wire-arc additive manufacturing. *Additive Manufacturing* 30: 100872.

2. Orzolek, S. M., Semple, J. K., and Fisher, C. R. 2021. Nickel-aluminum bronze (NAB) review: Additive manufacturing and weldability.

3. Kuprienko, A., Stickle, J., Harwig, D., Carney, M., and Fink, C. 2024. Effect of liquid nitrogen cryogenic cooling during wire arc directed energy deposition of nickel aluminum bronze. *Welding in the World* 68: 515–524.

4. Hyatt, C. V. 1997. Review of literature related to microstructure development during laser surface engineering of nickel aluminum bronze.

5. Orzolek, S. M., Semple, J. K., and Fisher, C. R. 2022. Influence of processing on the microstructure of nickel aluminum bronze (NAB). *Additive Manufacturing* 56: 102859.

6. Murray, T., Thomas, S., Wu, Y., Neil, W., and Hutchinson, C. 2020. Selective laser melting of nickel aluminium bronze. *Additive Manufacturing* 33: 101122.

7. Jia, Z., Wang, Z., Chen, M., Zhao, K., Sun, G., Han, H. E-. 2025. Tailoring microstructural evolution in laser deposited nickel-aluminum bronze alloy by controlling water cooling condition. *Journal of Materials Processing Technology* 335: 118659.

8. Hyatt, C. V., Magee, K., and Betancourt, T. 1998. The effect of heat input on the microstructure and properties of nickel aluminum bronze laser clad with a consumable of composition Cu-9.0 Al-4.6 Ni-3.9 Fe-1.2 Mn. *Metallurgical and Materials Transactions A* 29: 1677–1690.

9. Sriintharasut, S., Poopat, B., and Phung-on, I. 2018. The effects of different types of welding current on the characteristics of nickel aluminum bronze using gas metal arc welding. *Materials Today: Proceedings* 5: 9535–9542.

10. Li, B., Zheng, H., Han, C., and Zhou, K. 2021. Nanotwins-containing microstructure and superior mechanical strength of a Cu-9Al-5Fe-5Ni alloy additively manufactured by laser metal deposition. *Additive Manufacturing* 39: 101825.

11. Bellware, M. D. 1959. Weldability of nickel-aluminum bronze.

12. Guo, C., Hu, B., Wei, B., and Chen, F. 2022. Wire arc additive manufactured CuMn13Al7 high-manganese aluminium bronze. *Chinese Journal of Mechanical Engineering* 35: 110.

13. Rahni, M. M., Beidokhti, B., and Haddad-Sabzevar, M. 2017. Effect of filler metal on microstructure and mechanical properties of manganese-aluminum bronze repair welds. *Transactions of Nonferrous Metals Society of China* 27: 507–513.

14. Chakravarthy, M., Ramanaiah, N., and Rao, B. S. S. 2011. Effect of pulsing on mechanical properties of 90/10 and 70/30 CuNi alloy welds. *International Journal of Mechanical Engineering and Technology* 2: 52–62.

15. Devletian, J. H., Sullivan, M. J., and Engineer, C. W. 2006. Flux cored arc welding of CuNi 90/10 piping with CuNi 70/30 filler metal. Position Flux Cored Electrode Final Report, Portland State University.

16. Chakravarthy, M., Ramanaiah, N., and Sundara Siva Rao, B. 2014. Effect of laser welding on mechanical properties of 70/30 Cu-Ni alloy welds. *Proceedings of the Institution of Mechanical Engineers, Part B: Journal of Engineering Manufacture* 228: 1153–1161.

17. Garriott, F. E. 1952. Welding iron-bearing alpha aluminum bronze. *Welding Journal.*

18. Aguirre-Pulido, M., Verduzco-Martínez, J. A., Curiel-López, F. F., Lopez Morelos, V. H., Becerra, H. G. 2024. Microstructural characterization of MIG brazing ERCuAl cladding on API 5L X70 steel. *MRS Advances* 9: 1916–1922.

19. Tamilkolundhu, S., and Josephraj, F. X. 2025. Influence of CMT welding parameters on microstructural and properties investigation of dissimilar weld joint for aluminum bronze and carbon steel. *Materials Science and Technology* 41.

20. American Welding Society. 2015. Welding handbook: Materials and applications, Part 2.

21. Dawson, R. J. C. 1983. Welding of copper and copper base alloys. Welding Research Council Bulletin.

22. Feng, Z., Zacharia, T., and David, S. 1997. Thermal stress development in a nickel based superalloy during weldability test. *Welding Journal.*

23. Geerlings, H., Thomas, G., Clarke, A. J., Clarke, K., and Klemm-Toole, J. 2025. The effects of residual copper on laser-welded low-carbon sheet steels. *Welding Journa*l 104.

24. Kleindienst, J., Bagshaw, N., Iten, J., and Klemm-Toole, J. 2025. The effects of inoculation on the weldability of 6061 aluminum processed with GMA-DED. *Welding Journal* 104: 143s–153s. DOI: 10.29391/2025.104.017

25. McConville, D., Kleindienst, J., Bagshaw, N., Iten, J., Rafferty, B., and Klemm-Toole, J. 2026. An assessment of the reduction of solidification cracking in nickel and aluminum alloys modified for improved additive manufacturability.

26. Goodwin, G. 1987. Development of a new hot-cracking test — the Sigmajig. *Welding Journal* 66: 33s–38s.

27. Lippold, J., Shademan, S., and Baeslack, W. III. 1996. The effect of specimen strength and thickness on cracking susceptibility during the Sigmajig weldability test. *Welding Journal* 75.

28. Mossman, M., and Lippold, J. 2002. Weldability testing of dissimilar combinations of 5000- and 6000-series aluminum alloys. *Welding Journal* 81: 188s–194s.

29. Kou, S. 2015. A simple index for predicting the susceptibility to solidification cracking. *Welding Journal* 94: 374–388.

30. Kou, S. 2015. A criterion for cracking during solidification. *Acta Materialia* 88: 366–374.

31. Kleindienst, J., Bagshaw, N., Iten, J., and Klemm-Toole, J. 2025. Modeling solidification microstructure in an inoculated aluminum 6061 alloy processed with gas metal arc directed energy deposition. *JOM* 1–15.

32. Yang, S. W., Yeon, S. M., Jun, T. -S., Choi, D., Baek, H. S., Eo D. R., Lee, H., and Sohn, I. 2025. Investigation of bonding integrity and crack susceptibility in pure copper–STS 630 bimetallic structure fabricated by powder bed fusion. *Journal of Materials Research and Technology*.

33. Goodwin, G. 1988. The effects of heat input and weld process on hot cracking in stainless steel. *Welding Journal* 67: 88s–94s.

34. AWS A5 Committee on Filler Metal and Allied Materials. AWS A5.6. Specification for copper and copper-alloy electrodes for shielded metal arc welding. 9th ed. American Welding Society.

JOSEPH KLEINDIENST and **JONAH KLEMM-TOOLE** (*jklemmto@mines.edu*) are with the Colorado School of Mines, Golden, Colo. **DANIEL JAVERNICK** is with Los Alamos National Laboratory, Los Alamos, N.M.